Indonesian Journal of Material Research
e-ISSN: 2987-1654
Vol. 4, No. 3, November 2026

Indonesian Journal of MATERIAL RESEARCH

Research Paper

Preparing and Characterizing Porous MgO and NiO/MgO Nano-Compounds

Nguyen Thi Phuong Loan[1*]

[1] *Faculty of Fundamental 2, Posts and Telecommunications Institute of Technology, Ho Chi Minh City, 70000, Vietnam*
[*] **Corresponding author**: ntploan@ptithcm.edu.vn

Abstract
Porous MgO and NiO/MgO nanocomposites have attracted significant attention due to their potential applications in heterogeneous catalysis. In this study, MgO and NiO/MgO nanostructures were successfully synthesized using a modified citrate precursor method. The structural and textural properties of the obtained materials were characterized by X-ray diffraction (XRD), transmission electron microscopy (TEM), and nitrogen adsorption–desorption (BET) analysis. The results reveal that the synthesized MgO exhibits a high specific surface area of up to 230 m^2/g with particle sizes ranging from 5 to 20 nm. The incorporation of NiO into the mesoporous MgO matrix leads to changes in pore structure and particle growth behavior. The modified synthesis approach enables improved control over crystallite size and porosity compared to conventional methods. These findings suggest that the prepared materials are promising candidates for catalytic applications.

Keywords
MgO, NiO/MgO, Mesoporous Materials, Citrate Precursor Method, Nanostructures, Catalysis

Received: 27 January 2026, Accepted: 28 April 2026
https://doi.org/10.26554/ijmr.20264389

1. INTRODUCTION

Assisted oxide catalysts are frequently employed in a variety of catalytic procedures, hence they have been extensively studied. Assisted nickel catalysts are utilized in industrial processes to produce hydrogen and synthesized gas from hydrocarbon feedstock (Anh et al., 2025b; Anh and Lee, 2024). Ni/MgO is widely recognized as an effective nickel-based catalyst due to strong metal-support interaction, which suppresses sintering at high temperatures. Traditionally, Ni/MgO catalysts are impregnated in aqueous nickel salt solutions utilizing commercialized MgO help with a minimal surface area (about 100 m^2/g) (Ma et al., 2024; Sun et al., 2024). The MgO assistance and its primary purpose to serve as dispersing medium ought to have a large surface area. Specifically, the impact of surface area on catalyst action can be underestimated. MgO is typically synthesized by decomposing different magnesium salts (Phuong Loan and Quoc Anh, 2020; Loan and Anh, 2020a).

Recent studies have demonstrated that MgO plays a critical role in enhancing catalyst basicity and reducing carbon deposition, thereby improving catalytic performance and stability (Gao et al., 2024; Sun et al., 2026). Nevertheless, this approach results in MgO materials with large and diverse grain sizes, uneven forms, and limited surfaces, making them unsuitable for purposes. A cost-effective approach for producing nanosized MgO having a small size distribution and increased surface area is required. Sol-gel methods are being used effectively to create MgO powders with elevated surface area (Anh, 2024; Loan et al., 2026). We used an altered citrate precursor approach to create porous MgO and NiO/MgO nano-compounds having compact structures and elevated surface area. The process involves decomposing the citrate precursor of MgO and NiO/MgO powder in N_2 (0.5% O_2) before air annealing with reduced heat. This approach successfully regulated the crystallite diameter and surface area of the nanoparticles, according to subsequent experiments.

Although various methods such as sol-gel, precipitation, and hydrothermal synthesis have been widely reported for MgO-based materials, these approaches often suffer from limitations including poor control of particle size distribution and relatively low surface area. The citrate precursor method provides advantages such as homogeneous mixing at the molecular level and better stoichiometric control; however, conventional implementations still face challenges related to particle agglomeration and pore collapse during calcination.

In this work, a modified citrate precursor approach is employed to synthesize porous MgO and NiO/MgO nanocomposites with enhanced structural properties. The proposed method aims to improve pore formation and surface area while maintaining controlled crystallite growth. The relationship between synthesis parameters, microstructure, and textural properties is systematically investigated.

Compared to conventional citrate methods, the present approach provides improved control over pore formation and crystallite growth, resulting in higher surface area and more uniform nanostructures. In addition, the formation of NiO-MgO solid

solution has been reported to significantly improve metal dispersion and catalytic durability (Ling et al., 2024; Wang et al., 2024; Zhang et al., 2024).

2. EXPERIMENTAL SECTION

Magnesium nitrate ($Mg(NO_3)_2$), nickel nitrate ($Ni(NO_3)_2{\cdot}6H_2O$), and citric acid were used as starting materials without further purification. $Mg(NO_3)_2$ was dissolved in deionized water to form an aqueous solution, followed by the addition of citric acid under continuous stirring until a clear solution was obtained. The molar ratio between citric acid and metal cations (R) was adjusted to control the synthesis conditions. The solution was heated at approximately 80-90 °C under constant stirring to remove excess water and form a viscous gel. The gel was subsequently dried and calcined in a controlled atmosphere of N_2 containing 0.5% O_2 to obtain a MgO–carbon composite. Final crystallization was achieved by annealing in air for 3 hours. The effects of synthesis parameters, including the citrate-to-metal ratio and annealing temperature, were systematically investigated. For the preparation of NiO/MgO nanocomposites, MgO powder with a high surface area (~230 m^2/g) was impregnated with a nickel nitrate solution, followed by drying and calcination in air. X-ray diffraction (XRD) patterns were recorded using Cu Kα radiation with a step size of 0.02° and a scan rate of 0.3 s per step. Raman spectroscopy was used to analyze carbon species in intermediate products. Transmission electron microscopy (TEM) was performed at an acceleration voltage of 200 kV. Nitrogen adsorption–desorption measurements were conducted at 77 K, and the specific surface area was calculated using the BET method, while pore size distribution was determined using the BJH model (Li et al., 2026; Shu et al., 2026; Sun et al., 2026). The aforementioned characterizing data can be seen in Figure 1.

3. RESULT AND DISCUSSION

The XRD structures of powders having varied proportions (R = 1, 2) were calcined under 800°C during 1 hour in N_2 (0.5% O_2) are displayed in Figure 1(a), with a: R = 1, firing within N_2 (0.5% O_2) under 800°C; b: R = 2, firing within N_2 (0.5% O_2) under 800°C; c: R = 2, tempering within air under 400°C; d: R = 1, tempering within air under 400°C; e: R = 2, tempering within air under 500°C; f: R = 1 tempering within air under 500°C; g: NiO/MgO. The powders are amorphous and contain tiny crystallites measuring 3-4 nm. Raman spectroscopy was used to study the element of amorphous particles, as seen in Figure 1(b). Amorphous powders have Raman hue ranges. Two ranges were found at 1320 and 1595 cm^{-1}, which correspond to carbon ranges. MgO ranges were not observed, indicating that the formless MgO is carbon-encased. XRD structures of powders having an identical proportion annealed at various heats are presented, as well as powders with varied proportions annealed at identical heat. As the heat rises or the proportion falls, the widths narrow slightly. The crystallite dimensions were determined utilizing Scherrer's method based on the (2 0 0) diffracting peak and the half-width of diffracting peaks (Ho et al., 2024; Loan and Anh, 2020d; Thi et al., 2020). These values are comparable to previously reported MgO nanostructures synthesized via citrate-based methods, confirming the reliability of the present approach.

The average crystallite size (D) was estimated using the Scherrer equation:

$$D = \frac{K\lambda}{\beta \cos\theta} \tag{1}$$

where K is the shape factor, λ is the X-ray wavelength, β is the full width at half maximum (FWHM), and θ is the Bragg angle. The calculated crystallite sizes are consistent with the nanoscale range observed in TEM analysis, confirming the effectiveness of the synthesis method in controlling particle growth.

The results indicate that adjusting the synthesis parameters (temperature and citrate ratio) effectively controls the crystallite size. In comparison to the MgO specimen, the NiO/MgO's XRD structure exhibits no novel reflectance for NiO, save for higher peaks suggesting larger mean particle dimensions. The NiO/MgO mean particle dimension is 4 nm larger than the supporting (7 nm). NiO and MgO are face-centered cubic oxides with similar network factors (4.196 and 4.212 Å, correspondingly) and link lengths (2.10 and 2.11 Å, correspondingly). Therefore, MgO and NiO may create a solid mixture. In accordance with literature (Anh et al., 2025a; Loan and Anh, 2021), the XRD structures of two types of oxides show distinct peaks. MgO has a value of $2\theta \approx 62.64$ for the (2 2 0) face, while NiO has a 0.6° higher value. To compare, the BET surface area and pore dimension dispensations of MgO (identified as MgO(CC)) manufactured using the traditional citrate precursor approach were investigated as well, with data shown in Table 1.

The absence of distinct NiO diffraction peaks may indicate a high dispersion of Ni species within the MgO matrix or the possible formation of a solid solution. However, further characterization techniques such as X-ray photoelectron spectroscopy (XPS) or energy-dispersive X-ray mapping (EDX) are required to confirm this assumption. Similar behavior has been reported for NiO–MgO systems, where lattice similarity facilitates the formation of solid solutions and enhances catalytic performance (Chen et al., 2024; Chen and Huang, 2024; Mou et al., 2024). The forms of MgO and NiO/MgO specimens were seen using TEM. The forms of MgO and NiO/MgO specimens were seen using TEM in Figure 1(c). The TEM micrograph depicts a MgO specimen calcined in air over 3 hours. The TEM image shows that the powders are poly-crystals that form thin agglomerations. XRD analysis confirms the tiny size of the native particles. Agglomerations have many pores on their surface, potentially leading to a large surface area.

The intermediate structure has a homogeneous pore layout, suggesting a bowl-like structure. A TEM image of NiO/MgO catalysis substance is provided. A TEM image of NiO/MgO catalysis substance is provided in Figure 1(d). Following heating, NiO covered the spaces between particles and created a solid mixture with assistance, resulting in less visible pores on the agglomerations compared to MgO powders. The TEM image

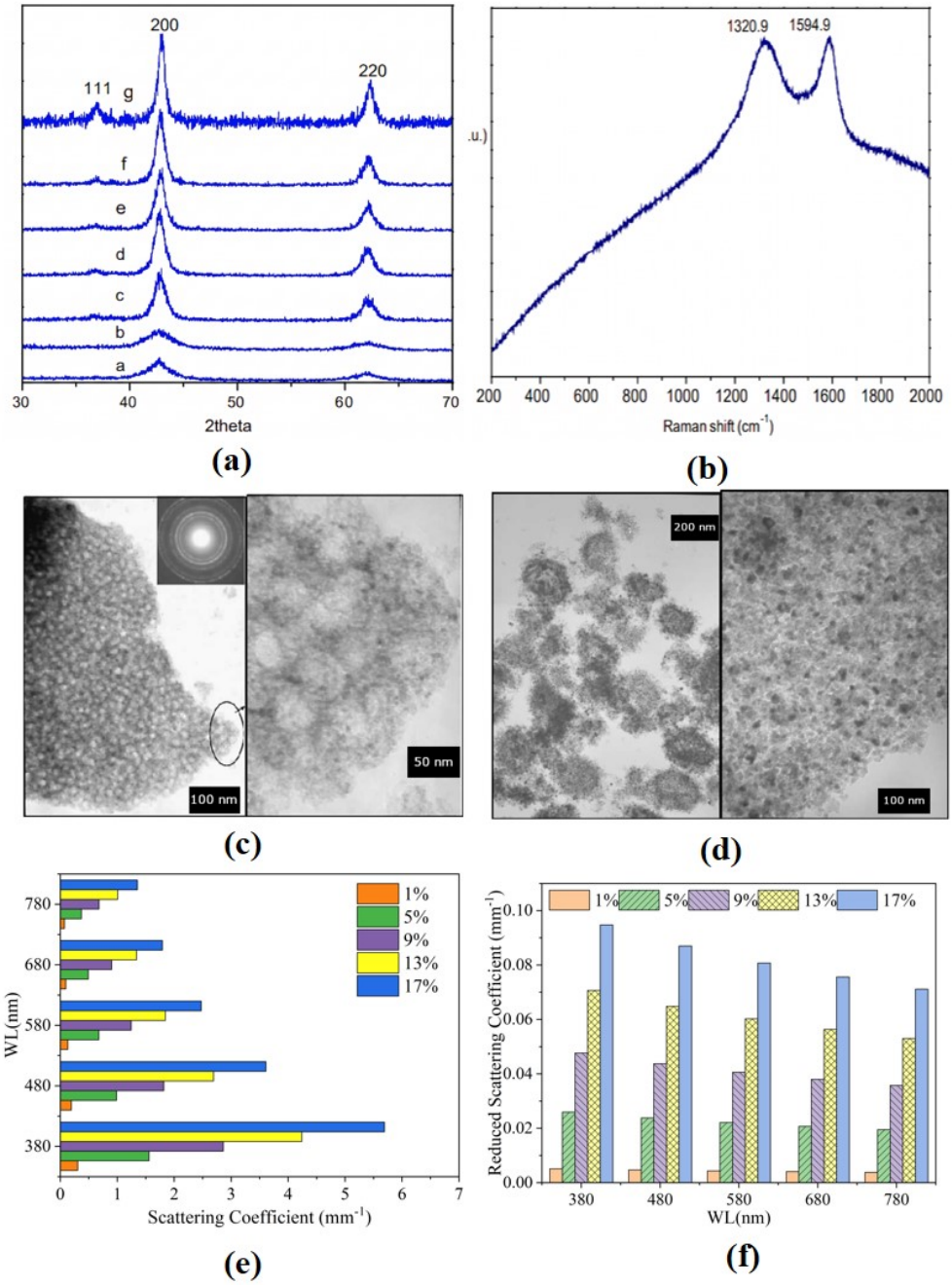

Figure 1. Characterizing Data of NiO/MgO Samples: (a) XRD, (b) Raman Spectra for Formless Powdered Samples Fired within N_2 (0.5% O_2) under 800°C, (c) TEM Visuals for MgO Having Ratio R of 2 tempered under 400°C, (d) TEM Visuals for NiO/MgO Catalytic Agents Fired under 500°C

shows homogenous black dots on the agglomerations' background, showing particle diameter dispersal. The particle size distribution estimated from TEM images indicates that the average particle size falls within the range of 5-20 nm, which is in good agreement with the XRD results. The relatively narrow size distribution suggests that the modified citrate precursor method effectively controls particle growth and aggregation.

The N_2 adsorbing-desorbing isotherm for the MgO specimen having the proportion of R = 2 annealed during 3 hours, indicating the specimen has the largest surface area. The N_2 adsorbing-desorbing isotherm for NiO/MgO nano-compounds was additionally presented. The pore dimension distributions were calculated employing the Barrett-Joyner-Halenda (BJH) approach and the Halsey formula for multi-sheet thickness (Chan

Table 1. Pattern attributes in MgO as well as NiO/MgO samples

Sample	S_{BET} (m^2/g)	Pore volume (cm^3/g)	Average pore sizes (nm)
MgO (MC)	230	0.27	4.0
MgO (CC)	70	0.24	8.8
NiO/MgO	50	0.22	5.3

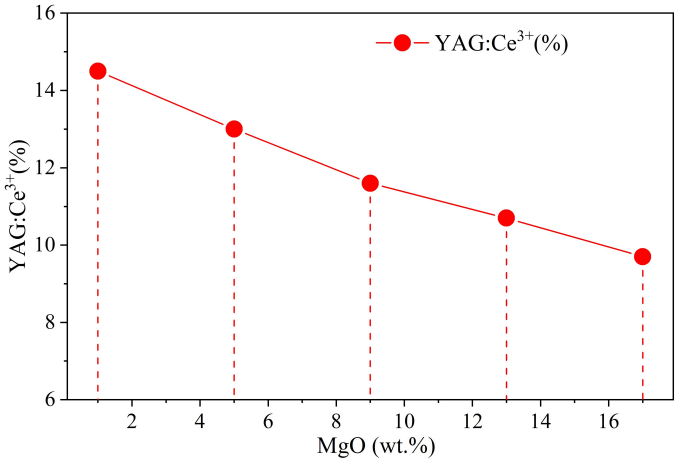

Figure 2. YAG:Ce Phosphor Proportion Values with Different MgO Proportions

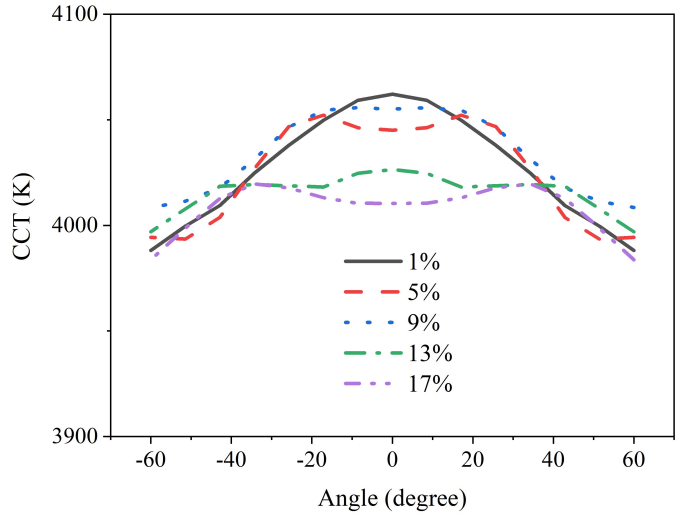

Figure 3. CCT Values with Various MgO Proportions

et al., 2024; Wang et al., 2025; Wei et al., 2024). The maximum is in the mesoporous region, with a limit maximum of 40 Å. The major maximum is in the mesoporous region, having a limit maximum of 52 Å. In addition to the main highest point, we found a smaller highest point at 135 Å. We found two major pore diameters in our specimens, despite their heterogeneity. To compare, the surface area and pore dimension dispensations of MgO (identified as MgO(CC)) manufactured using the traditional

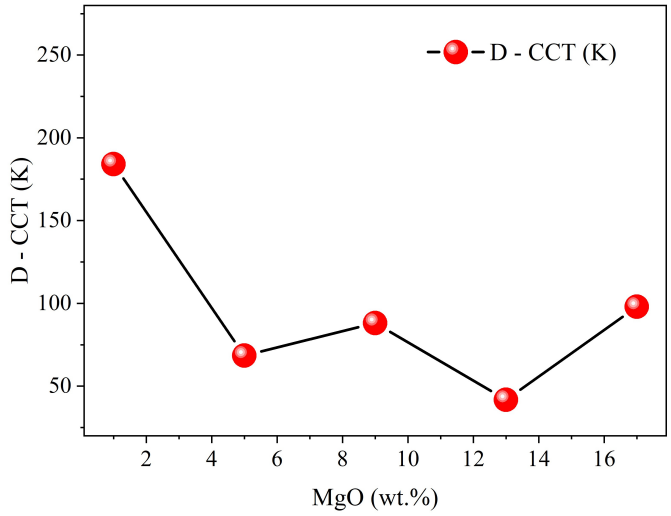

Figure 4. Color Difference Values with Different MgO Proportions

citrate precursor approach were investigated as well.

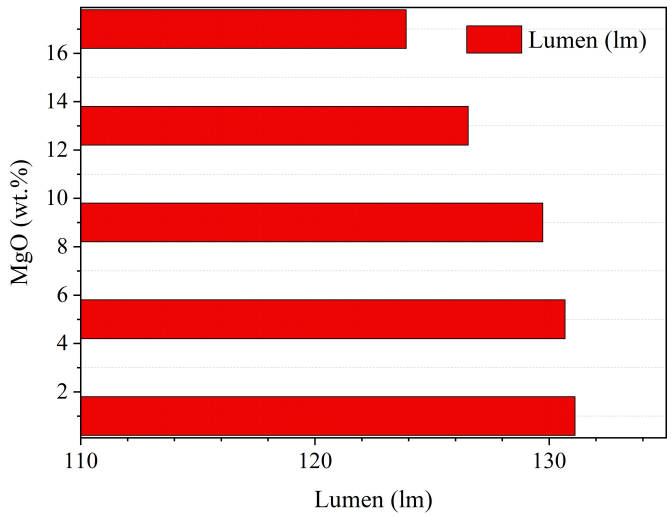

Figure 5. Luminescence Strength with Various MgO Proportions

Introducing NiO decreases the surface area and quantity, but increases the pore sizes. Loading 24 wt.% NiO into the mesoporous form results in a rise in wall thickness, leading to a

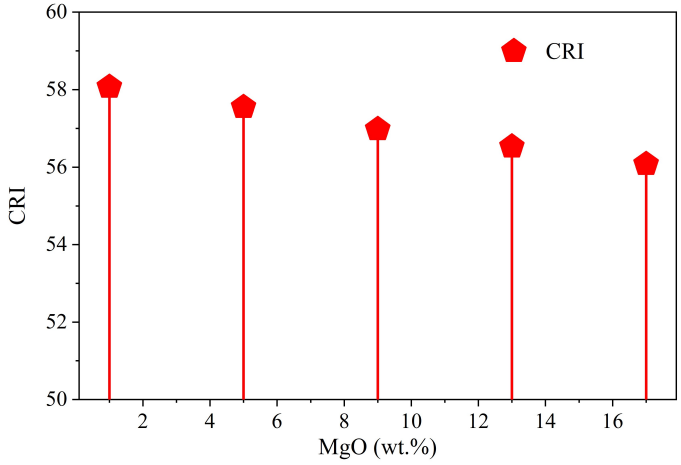

Figure 6. CRI Values with Various MgO Proportions

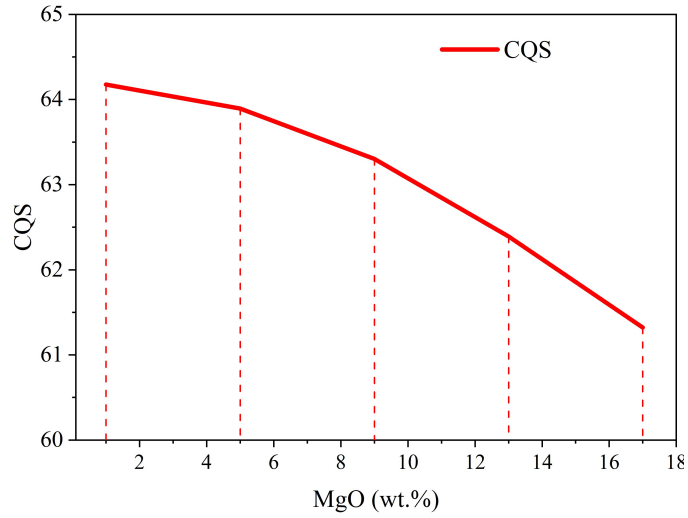

Figure 7. CQS Values with Various MgO Proportions

decrease in the outermost region and mass. Introducing NiO results in a size rise, indicating that it is absorbed into the intermediate structure rather than being placed as nanoparticles on the channel walls. This modification has a small effect on pore diameter but significantly reduces the surface area and quantity (Loan and Anh, 2020c; That and Anh, 2021; My et al., 2022). The decrease in specific surface area after NiO incorporation can be attributed to partial pore blockage and increased wall thickness within the mesoporous structure. In addition, the shift in pore size distribution suggests that Ni species are not only deposited on the surface but may also penetrate into the pore channels, leading to structural modification of the MgO framework.

The citrate precursor approach is commonly employed to produce nano-metered oxide due to its benefits, including homogeneous combining at the atomic scale, accurate stoichiometry, ease of operation, and inexpensive reagent expenses. The approach involves immediately calcining metal oxide precursors in air, which disintegrate into carbon dioxide, water, carbon monoxide, and metal oxide in the existence of oxygen. Uncontrolled oxidation of organic molecules leads to excessive heat and elevated local temperatures. Particles tend to be large and have little surface area. Subsequently thermal process, carbons are softly oxidized in air at low temperatures, resulting in the final crystalline of MgO. The pores were created through the burning of carbons, containing amorphous MgO. Earlier research suggests an elevated level of citric acid or an environment that prevents carbon oxidation may delay the crystallize process of the required oxide stage of polymeric precursors (Tran et al., 2020; Loan and Anh, 2021; That and Anh, 2021). Metal oxides created using the citrate approach tend to have larger particle sizes when their proportion rises, according to some research. Burning an amorphous combination of specimens having varying carbon ratios validated their impact on crystallization. The XRD structure of the specimen (R = 1) showed more powerful and highest peaks compared to the specimen (R = 2) annealed at the identical heat. Lower carbon content leads to higher crystallization and larger particles.

Figure 1 illustrates the relationship between MgO dose and light dispersion. It has the potential to boost MgO dosages by improving light transmission and wavelength conversion efficiency. Blue light brightness may increase when forward scattering and reabsorption decrease, but forward emission blue light dispersion increases. This is accomplished by increasing the concentration of MgO while decreasing the amount of yellow phosphorus. Similarly, the ability to choose the correct color temperature (CCT) is limited. Figures 3 and 4 show that CCT is concentration independent; nevertheless, as the dosage of MgO increases, so does the dosage of YGA:Ce yellow phosphor, as shown in Figure 2. Figure 2 reveals that increasing MgO doses (1-17 wt.%) reduces YGA:Ce phosphor ratios (from about 15% to just about 10%). Figure 3 shows how increasing doping reduces a phosphor's CCT variance. CCT values peak at temperatures greater than 4050 K and MgO concentrations of 1 wt.%. According to Figure 4, the D-CCT ultimately achieves its lowest value at 13 wt.% MgO, which is about 130 K lower than the greatest value at 1 wt.% MgO, which is around 180 K.

Figure 5 shows that MgO does not always improve the brightness of white light emissions. The highest results were obtained at a MgO concentration of 1 wt.%, while the lowest were at a concentration of 17 wt.%. Increased backscattering and reabsorption result in reduced blue emission and an uneven distribution of hues (Le et al., 2025; Loan and Anh, 2020b; Trang and Anh, 2025). When subjected to more backscattered blue light, increased MgO concentrations can cause the phosphor to shift color from blue to yellow or orange-red. Before the phosphor coating may expand, a particular amount of MgO must exist. The emission spectrum would be narrowed due to the multiple reflections obtained by the altered light from various objects. In other words, a high phosphor dose may increase the proportion of converted light that is reflected back, hence increasing CCT while decreasing luminous intensity. Figure 5 shows how adding 1 wt.% MgO to a simulated WLED with a lumen output power greater than 130

lm increases brightness and color uniformity (Cong and Anh, 2025; Loan et al., 2025; Van Dung and Anh, 2025).

Figures 6 and 7 show how the concentration of MgO affects the brightness and hue rendition of white LEDs. Experiments with color rendition utilizing the color rendering indicator (CRI) and the color quality scale (CQS) revealed a steady reduction as the MgO concentration grew to 17 wt.%. CRI and CQS declines may be attributed to the unpredictable character of blue, green, and yellow-orange colors (Cong and Anh, 2025; Loan and Anh, 2020b; Trang and Anh, 2025). High amounts of MgO generate irregular light emission, a bias toward the yellow-orange spectrum, and increased dispersion. As we investigate the results, we will adjust the CRI and CQS of this phosphor, as well as take into account other characteristics such as particle size.

4. CONCLUSIONS

In this study, porous MgO and NiO/MgO nanocomposites were successfully synthesized using a modified citrate precursor method. The results demonstrate that synthesis parameters, particularly the citrate-to-metal ratio and annealing conditions, play a key role in controlling crystallite size and surface area. The prepared MgO exhibits a high specific surface area of up to 230 m^2/g and a well-developed mesoporous structure. The incorporation of NiO leads to structural modifications, including reduced surface area and changes in pore size distribution. Although the formation of a solid solution between NiO and MgO is suggested, additional characterization is required for confirmation. The developed materials show promising potential for catalytic applications due to their tunable structural and textural properties. This study provides useful insights into the design of high-surface-area MgO-based materials for catalytic applications. Future work will focus on evaluating the catalytic performance of the prepared materials in relevant reactions such as steam reforming to further validate their practical applicability.

5. ACKNOWLEDGEMENT

The authors wish to express their gratitude to the Posts and Telecommunications Institute of Technology, Vietnam, for financial support for this research.

REFERENCES

Anh, N. and H. Lee (2024). Titanium Dioxide in Vanadate Red Phosphor Compound for Conventional White Light Emitting Diodes. *Optoelectronics and Advanced Materials-Rapid Communications*, **18**(September-October 2024); 480–484

Anh, N. D. Q. (2024). Nano Scattering Particle: An Approach to Improve Quality of the Commercial Led. *The University of Danang - Journal of Science and Technology*; 53–57

Anh, N. D. Q., S. D. Ho, P. T. M. Man, T. K. Duy, and N. T. P. Loan (2025a). Obtaining Higher LED's Lighting Chromaticity and Luminosity with SiO_2 Particles at Different Diameters. *Journal of Advanced Engineering and Computation*, **9**(1); 21–28

Anh, N. D. Q., N. T. P. Loan, P. VAN DE, and H.-Y. Lee (2025b). Potassium Bromide Scattering Simulation for Improving Phosphor-converting White LED Performance. *Optoelectronics and Advanced Materials-Rapid Communications*, **19**(July-August 2025); 378–383

Chan, J., B. Devakumar, H. Gao, and X. Huang (2024). Efficient Violet-Light-Excitable Blue-Cyan-Emitting $Ca_2YHf_2GaAl_2O_{12}$: Ce^{3+} garnet phosphors enable high-color-rendering full-spectrum warm-white LEDs. *Materials Today Chemistry*, **40**; 102218

Chen, S., H. Li, and X. Wang (2024). Recent Advances in NiO−MgO Solid Solution Catalysts for Hydrogen Production. *Journal of Catalysis*, **428**; 152–165

Chen, X. and X. Huang (2024). Highly Efficient Blue-Light-Excitable Ultra-Broadband Orange-Emitting $Mg_{2.5}Y_{1.5}Al_{1.5}Si_{2.5}O_{12}$: Ce^{3+} Garnet Phosphors for Solid-State Lighting. *Journal of Alloys and Compounds*, **997**; 174906

Cong, P. H. and N. D. Q. Anh (2025). Augmenting Chroma Performance for WLED Employing $Sr_8ZnSc(PO_4)_7$: Eu^{2+}@ SiO_2 as a Scattering-Enhancing Substance. *Science and Technology Indonesia*, **10**(2); 467–472

Gao, D., Z. Wang, X. Zhang, Q. Pang, and X. Wang (2024). High-Throughput Information Storage in an Intelligent Response Phosphor. *ACS Applied Materials & Interfaces*, **17**(2); 3587–3596

Ho, S. D., N. T. P. Loan, H. Y. Lee, and N. D. Q. Anh (2024). Study of K_2SiF_6: Mn^{4+}@ SiO_2 Phosphor for White LEDs with High Angular Color Uniformity. *Journal of Advanced Engineering and Computation*, **8**(1); 53–62

Le, P., N. Loan, N. Anh, and H. Lee (2025). Thermally Stable Sol-Gel Yttrium Aluminum Garnet Cerium Phosphors for White Light-Emitting Diodes. *International Journal of Advances in Applied Sciences*, **14**(4); 1367

Li, Z., Y. Gong, Z. Zhang, Z. Lu, Y. Shi, G. Yan, L. Zhuo, and G. Zhang (2026). Isovalent Ti^{4+} Doping Synergistically Enhances Mechanical Strength and CO_2 Capture of Li_4SiO_4 Pebbles: A Contrast with ZrO_2-Doped Systems. *Journal of Industrial and Engineering Chemistry*

Ling, J., Y. Zhou, C. Lin, H. Zhang, W. Xu, and M. Hong (2024). Spectrum Regulation of LuAG: Ce Phosphor Ceramic with Gd Doping for High-brightness and High-power Yellow-emitting LEDs Applications. *Journal of the European Ceramic Society*, **44**(11); 6430–6440

Loan, N. and N. Anh (2021). Enhancing Optical Performance of Dual-Layer Remote Phosphor Structures with the Application of $LaAsO_4$: Eu^{3+} and Y_2O_3: Ho^{3+}. *Optoelectronics and Advanced Materials-Rapid Communications*, **15**(January-February 2021); 71–78

Loan, N., N. Anh, P. Man, and H. Lee (2025). Assessing Thermic Degradation for Yttrium–Aluminum Precursive Agents Applied to YAG Phosphor Samples. *Science and Technology Indonesia*, **10**(4); 1209–1214

Loan, N. T. P. and N. D. Q. Anh (2020a). $LaSiO_3Cl$: Ce^{3+}, Tb^{3+} and Mg_2TiO_4: Mn^{4+}: Quantum Dot Phosphors for Improving the Optical Properties of WLEDs. *International Journal of Electrical & Computer Engineering (2088-8708)*, **10**(5)

Loan, N. T. P. and N. D. Q. Anh (2020b). $SrBaSiO_4$: Eu^{2+} Phosphor: a Novel Application for Improving the Luminous Flux and Color Quality of Multi-Chip White LED Lamps. *International Journal of Electrical and Computer Engineering (IJECE)*, **10**(5); 5147–5154

Loan, N. T. P. and N. D. Q. Anh (2020c). Utilizing $CaCO_3$, CaF_2, SiO_2, and TiO_2 Particles to Enhance Color Homogeneity and Luminous Flux of WLEDs. *International Journal of Electrical & Computer Engineering (2088-8708)*, **10**(5); 5175

Loan, N. T. P. and N. D. Q. Anh (2020d). Y_2O_3: Ho^{3+} and ZnO: Bi^{3+}: A Selection for Enhancing Color Quality and Luminous Flux of WLEDs. *International Journal of Electrical & Computer Engineering (2088-8708)*, **10**(5); 5162–5167

Loan, N. T. P., P. X. Le, and P. T. M. Man (2026). Non-Proximity as Well as Immediate Tracking for Phosphor Heat Within Phosphor-Transmuted WLED Apparatuses. *Indonesian Journal of Material Research*, **4**(2); 56–61

Ma, Y., Z. Wang, T. Pang, S. Lin, L. Wu, G. Xi, L. Zeng, L. Lu, Y. Fu, and Y. Tian (2024). A Cyan-Green-Emitting Garnet-Structured $Lu_{3-x}Sc_xAl_{2-y}Sc_yAl_{3-z}Sc_zO_{12}$: Ce^{3+} Phosphor Ceramics Towards High-Color-Quality Laser-Driven Lighting. *Ceramics International*, **50**(12); 21074–21082

Mou, Y., B. Tian, X. Liu, J. Zhao, X. Wang, D. Chen, J. Xu, X. Wang, and Y. Peng (2024). High Color Quality Laser-Driven White Lighting Enabled by Reflective Bicolor Phosphor-in-Glass Film Converter. *Journal of Rare Earths*, **43**(9); 1844–1851

My, L. T. T., N. L. Thai, T. M. Bui, H.-Y. Lee, and N. D. Q. Anh (2022). Phosphor Conversion for WLEDs: YBO_3: Ce^{3+}, Tb^{3+} and Its Effects on the Luminous Intensity and Chromatic Properties of Dual-layer Wled Model. *Materials Science Poland*, **40**(4); 105–113

Phuong Loan, N. T. and N. D. Quoc Anh (2020). The Effectiveness of $MgCeAl_{11}O_{19}$: Tb^{3+} Phosphor in Enhancing the Luminous Efficacy and Color Quality of Multi-Chip White LEDs. *International Journal of Electrical & Computer Engineering (2088-8708)*, **10**(5); 4631–4638

Shu, P., Y. Ma, W. Liu, J. Wang, and S. Yao (2026). Mechanisms and Influences of Sc_2O_3 Doping on the Structural Evolution and Properties of Al_2O_3-ZrO_2 Fibers. *Ceramics International*

Sun, J., X. Gao, L. Zhang, W. Shi, S. Liu, X. Jia, L. Luo, and Q. Wang (2026). Interfacial Synergistic Effects in ZrO_2-Reinforced PDMS Coatings: Achieving Durable Easy-Cleaning Performance at Elevated Temperatures. *Materialia*; 102732

Sun, X., Y. Liang, J. Zheng, C. Zhao, Z. Fang, T. Tian, X. Liang, W. Huan, and W. Xiang (2024). Advancing Laser Lighting: High-Brightness and High-Stability Ce: YAG Phosphor-in-Glass. *Ceramics International*, **50**(23); 48909–48917

That, P. T. and N. Đ. Q. Anh (2021). Green $Ca_2La_2BO_{6.5}$: Pb_{2+} Phosphor: an Innovative Solution in Enhancing the Color Quality and Luminous Flux of WLEDs. *TELKOMNIKA (Telecommunication Computing Electronics and Control)*, **19**(5); 1630–1635

Thi, M. H. N., N. T. P. Loan, and N. D. Q. Anh (2020). Study of Red-emitting $LaAsO_4$: Eu^{3+} Phosphor for Color Rendering Index Improvement of WLEDs with Dual-layer Remote Phosphor Geometry. *TELKOMNIKA (Telecommunication Computing Electronics and Control)*, **18**(6); 3210

Tran, A.-M. D., N. D. Q. Anh, and N. T. P. Loan (2020). Enhancing Light Sources Color Homogeneity in High-power Phosphor-based White LED Using ZnO Particles. *TELKOMNIKA (Telecommunication Computing Electronics and Control)*, **18**(5); 2628–2634

Trang, L. and N. Anh (2025). Influences from SiO_2 Particles on Optical Properties of White Diodes Verified Through Computer Simulation. *Indonesian Journal of Electrical Engineering and Computer Science*, **38**(3); 1572–1579

Van Dung, N. and N. D. Q. Anh (2025). $Ba_3GdNa(PO_4)_3F$: Eu^{2+} Phosphor with Blue-Red Emission Colors on White-LED Properties. *Indonesian Journal of Electrical Engineering and Computer Science*, **38**(3); 1564–1571

Wang, Y., Z. Cheng, J. Ye, D. Zhu, C. Hu, Z. Zhou, T. Li, W. Chewpraditkul, K. Sreebunpeng, and W. Chewpraditkulb (2025). Effect of Ga^{3+} Content on the Luminous Properties of Ce^{3+}-Doped $Lu_2YGa_xAl_{5-x}O_{12}$ Phosphor Ceramics for Potential Lighting Application. *Journal of Luminescence*, **280**; 121115

Wang, Y., J. Liu, and Z. Zhang (2024). Mesoporous MgO Materials with High Surface Area for Catalytic Applications. *Materials Chemistry and Physics*, **312**; 128765

Wei, C., J. Kang, C. Shao, P. Sang, T. Zhou, M. Li, F. Qiu, B. Jiang, R. Xu, and W. Strek (2024). Enhanced Efficiency and Thermal Performance of Multistage Gradient Doping Ce: YAG Transparent Ceramics for Laser Lighting. *Journal of the European Ceramic Society*, **44**(10); 5804–5813

Zhang, B., J. Zhou, W. Zhu, F. Huang, R. Ye, H. Ma, Y. Hua, and S. Xu (2024). Robust High-Efficiency LuAG: Ce Phosphor-in-Silica Glass (PiSG) for High-Brightness Laser Lighting. *Ceramics International*, **50**(3); 5868–5876

